RESEARCH ARTICLE

Facet {100} Fosters Resonance Energy Transfer in Ni/Co-doped $CsPbBr_3$ Nanocrystals

Suvadeep Panda[1], Gourab Roy[1], Tathamay Basu[1], Debashis Panda[1]*

[1] Department of Sciences & Humanities
Rajiv Gandhi Institute of Petroleum Technology,
An Institution of National Importance, Govt. of India
Jais, Uttar Pradesh, INDIA

Email: dpanda@rgipt.ac.in
Phone: +91 9455196041.

Supporting information for this manuscript is also available.

Abstract:

The design of an effective light harvester with metal-doped perovskite nanocrystals (M:PNCs) aims at achieving directional energy flow. The potential of crystal facets needs to be assessed for dictating energy transfer dynamics of M:PNCs. Herein we have engineered facets of amine-capped $CsPbBr_3$ perovskite nanocrystals by doping with a trace amount of Ni and Co ions. Ni-doped $CsPbBr_3$ (Ni:PNC) showcases structural heterogeneity with regular cubic and rod shapes whereas bimetallic-doped $CsPbBr_3$ (Ni:Co:PNC) evolves to an elongated dodecahedron structure. Structural analysis using Rietveld Refinement strongly corroborates the construction of dodecahedron structure for Ni:Co:PNC through systematic displacement of Cs ions. Energy transfer from doped nanocrystals to Rhodamine B (RhB) occurs through dipole-dipole interaction, known as Fluorescence Resonance Energy Transfer (FRET). The emergence of isoemissive point, and rise-time of RhB conclusively establish Resonance Energy Transfer mechanism. Energy transfer in thin films occurs at much faster rate than in toluene medium. {100} facet-dominated Ni:PNC registers a FRET efficiency of 94% whereas {111}, {002} facet-dominated Ni:Co:PNC restricts at 21% FRET efficiency. The distance between donor and acceptor, R_{DA} dictates the dynamics of energy transfer, rather than spectral overlap, and photoluminescence quantum yield of these doped-nanocrystals. Surface composition of facets, typically Cs ions perhaps plays a decisive role in regulating the binding constant of donor and acceptor. Our study demonstrates the importance of facets of nanocrystals in tuning the desired energy transfer processes for photocatalytic applications.

1. Introduction:

Colloidal cesium lead halide perovskite ($CsPbX_3$, X = Cl, Br, I) nanocrystals (PNCs) are the most promising photoluminescent inorganic self-assemblies owing to their cutting-edge applications in tandem-solar cell, light-emitting diodes and photo(electro)catalysis.[1–4] However, these photoluminescent nanocrystals remain far from practical applicability due to their poor ambient stability.[5–7] Coulombic interaction guided dynamic binding between ammonium ions (of oleylamine) with bromide ions present in crystal lattice and oleate ions (of oleic acid) with lattice's cesium ions falls apart in presence of water molecule, as oleate becomes oleic acid and leaves hydroxide ion. This hydroxide ion readily forms lead hydroxide salt, $Pb(OH)_2$ with crystal's Pb(II) ion.[8] Very recently Ma et al. have elucidated the intricacies of binding water molecules with formamidinium lead iodide ($FAPbI_3$) nanocrystal and demonstrated that its crystal facet {100} is substantially more vulnerable to moisture-induced degradation than facet {111}.[9] To improve the ambient stability of PNCs, doping of metal ions into perovskite crystal is in current focus of research.[10–12]

Metal ion-doped perovskite nanocrystals (M:PNCs) possess unique excellent photostability (PL), narrow spectral widths, and bandgap tunability. Very recently, doping of several alkaline-earth metals (e.g., Mg^{2+}, Ca^{2+}, and Ba^{2+}) into perovskite nanocrystals have been investigated for improvement of photoluminescence quantum yield.[13–15] Transition metal ions have also been tested as dopants for achieving near-unity photoluminescence quantum yield, band tuning and improving stability. [16–19] The defect tolerance ability of PNCs remains the foundation behind such doping.[20] However, a greater emphasis on sustainability vis-à-vis Net-Zero carbon emission has also pushed researchers to harness the potential of metal-doped perovskite nanocrystals for

photocatalytic applications- such as, green hydrogen production and sustainable fuels/chemicals production by CO_2 reduction.[21–25]

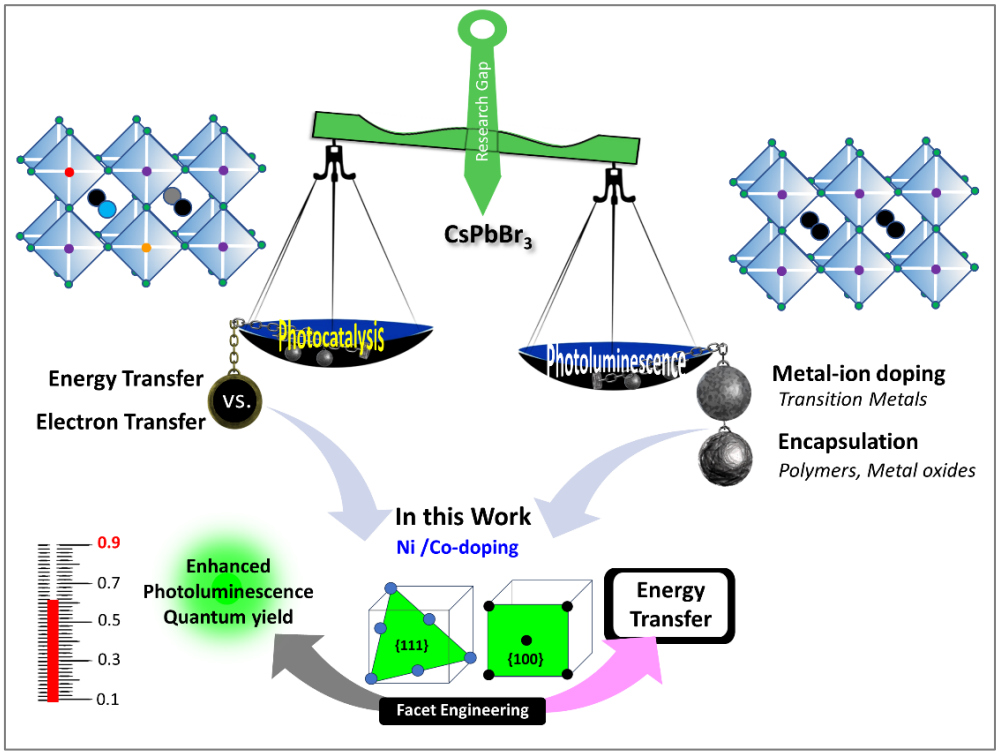

Scheme 1: Highlighting the research gap and scope of our work in deciphering facet-directed energy transfer dynamics of transition metal-doped Cesium lead halide perovskite nanocrystal (M:PNC).

Efficient energy transfer coupled with electron transfer remains the bottleneck in designing of a semiconductor photocatalysts with augmented photocatalytic efficiency.[26–28] In order to achieve so, doping of catalytically active transition metal ions (Pd, Fe, Cu, etc.) is done quite frequently with a presumption that these ions can facilitate electron (charge) transfer processes. [23,29,30] However, the complexity involved in excited state energy transfer processes of transition-metal ion doped nanocrystals are not investigated in detail. Thus, it has intrigued us to investigate the photophysics and photochemistry of Nickel(II) and Cobalt(II) ions-doped cesium lead bromide nanocrystals (**Scheme 1**). Ni(II) ion doped nanocrystals are found to retain intense emission and offer remarkable stability. The role of dopant, Ni(II) ions having the smallest transition metal

Shannon radii in modulating photoluminescence properties of perovskite nanocrystal has been attributed to structural rigidity of crystal favoring carrier-dopant spin exchange interactions.[31,32] Here, we have selected Ni / Co-doped nanocrystal as a donor and organic dye, Rhodamine B as an acceptor for understanding the energy transfer processes. The basis of this donor-acceptor selection stems from the observation of photocurrent generation by organic dyes in quantum dot solar cells.[33,34] Moreover, recent studies on Förster Resonance Energy Transfer (FRET) between pristine cesium lead bromide perovskite and organic fluorophores indicate that singlet energy transfer efficiency is dictated by- (i) binding constant of acceptor with nanocrystal's surface, and (ii) overlap integral, J(λ).[35–37] Binding constant of a donor-acceptor system is very intrinsic and thus plays a pivotal role in determining the efficiency of energy transfer, whereas overlap integral, a theoretical concept provides a rationale for modulation of energy transfer efficiency for a set of systems. However, it has been presumed that donor-acceptance remains unchanged. Thus, it is pertinent to understand the role of crystal facets in regulating the binding constant vis-à-vis energy transfer from transition metal-ion doped perovskite nanocrystal to organic fluorophore.[38]

In this work, we have synthesized Ni:$CsPbBr_3$ (Ni:PNC) and Co:$CsPbBr_3$ (Co:PNC) and Ni:Co:$CsPbBr_3$ (Ni:Co:PNC) perovskite nanocrystals by using a modified hot-injection method. And to decipher the role of crystal facets in energy transfer, we have selected an organic dye, Rhodamine B as an acceptor, whose photophysical properties are well characterized.[39] The reason for selection for these donors (D) -acceptor (A) pair is owing to nearly identical values of spectral overlap integral, J(λ) between emission of metal-doped PNCs (M:PNCs) and absorption of Rhodamine B (RhB).

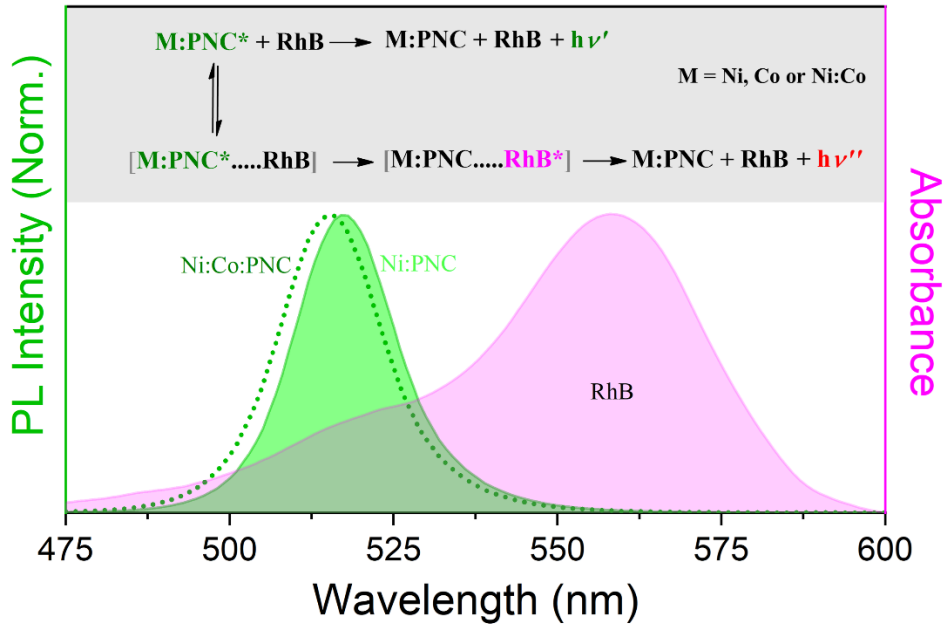

Scheme 2: Spectral overlap between photoluminescence spectra of metal-doped PNCs and Rhodamine B. Energy transfer processes involved between M:PNCs and Rhodamine B, where hν′ is the emission from metal-doped PNC and hν″ is the emission from Rhodamine B and * indicates the excited state.

Energy transfer from M:PNCs to Rhodamine B is probed by the decrease in emission of PNCs and concurrent increased emission of RhB. And the appearance of iso-emissive point is suggestive of equilibrium between two emissive species (**Scheme 2**). Herein energy transfer from metal-doped perovskite nanocrystals to Rhodamine B has been systematically investigated by using steady state and time-resolved photoluminescence measurements. Our detailed structural studies document the crystal stiffening by a small doping of Ni/Co which modifies the facet accordingly. We believe this study will serve as a rule of thumb for designing a transition metal-doped perovskite nanocrystals for tuning their photocatalytic activities.

2. Materials & Methods:

Materials. Lead Bromide ($PbBr_2$, 99%, Molychem), Cesium Carbonate (Cs_2CO_3, 97%, SRL Chem), Nickel Acetate Tetrahydrate ($(CH_3COO)_2Ni\ 4H_2O$,98%, Molychem), Cobalt Acetate Tetrahydrate ($(CH_3COO)_2Co.4H_2O$, 99%, Molychem),1-Octadecene (ODE,90%, TCI Chemicals), Oleic Acid (OA, Molychem), Oleylamine (OAm, 95%, SRL Chem), Hexane HPLC (95%, Molychem),Toluene HPLC (99.8% Molychem), Rhodamine B (Molychem). Acetonitrile HPLC (99.8%, SDFCL) All reagents were used without any further purification.

Synthesis of Metal (Ni, Co)-doped Perovskite Nanocrystals (M:PNC): For the synthesis of Cesium−Oleate precursor, first, cesium carbonate (1.31 g), oleic acid (4 mL), and octadecene (16 mL) are mixed in a 100 mL three-neck round-bottom flask and then kept in a vacuum oven for 15 min (120^{o}C, -700 mmHg). The solution mixture is heated to 120 °C under vigorous stirring for 60 min while purging with N_2 gas to remove the moisture. Afterward, the mixture is heated to 150 °C until the solution became transparent brown colour indicating formation of Cesium Oleate. In a typical synthesis of metal doped-$CsPbBr_3$ nanocrystal, oleic acid (6 mL), oleylamine (6 mL), and octadecene (9 mL) are taken in a 100 mL three-neck round-bottom flask and dried under vacuum for 30 min at 120 °C to remove the moisture content from the above chemicals. For synthesis of pristine PNC— 1.0 g of $PbBr_2$ while for Ni:PNC — 1.0 g of $PbBr_2$ (2.8 mmol), 250 mg Nickel (II) acetate (1.0 mmol); for Co:PNC— 1.0 g of $PbBr_2$ (2.8 mmol), 250 mg Cobalt (II) acetate (1.0 mmol) and for bimetallic doped, Ni:Co:PNC— 1.0 g of $PbBr_2$ (2.8 mmol), 125 mg Nickel (II) acetate, 125 mg Cobalt (II) acetate (1.0 mmol) are dissolved completely by heating the solution at 150 °C. The temperature is then elevated to 180°C and 5 mL of Cs−oleate precursor is swiftly injected under vigorous stirring. After 10s, the reaction mixture is transferred into an ice bath, then a greenish-yellow precipitate is obtained. The precipitate is first centrifuged

at 10000 rpm for 5 min to discard oils and then redispersed solution is again centrifuged at 10000 rpm for 10 min to remove large-sized particles. The synthesized PNCs are used for further experimentation.

Reitveld Refinement Process: Rietveld refinement entails adjusting various parameters describing the diffraction pattern to align with observed data by fitting a calculated X-ray or neutron diffraction pattern.[40] Initially, a theoretical diffraction pattern is computed using the initial structural model. To assess the fit quality between calculated and experimental patterns, statistical measures such as Rietveld refinement factors are employed, offering insights into the adequacy of the refined structural model.[41] In a typical Rietveld refinement, individual scale factors pertaining to phase concentration, as well as profile, background, and lattice parameters, are variably adjusted. The refinement process is iterative, with parameters readjusted until convergence between calculated and experimental patterns occurs, stabilizing refinement parameters. Upon achieving a satisfactory fit, the refined structural model furnishes precise information regarding the material's crystal structure, encompassing atomic positions, unit cell dimensions, bond lengths, bond angles, and other structural parameters. In Rietveld refinement, the χ^2 statistic is a measure of the goodness of fit between the observed diffraction data and the calculated diffraction pattern.

In the Rietveld refinement process a two-phase approach is adopted, considering the presence of both orthorhombic and cubic phases simultaneously. The orthorhombic phase belongs to the pnma space group, while the cubic phase is classified under the Pm-3m space group. During the refinement process, we have employed a background model based on "Linear interpolation between a set background points with refinable heights." Additionally, the peak shape was modeled using the "Thompson-Cox Hastings pseudo-Voigt Axial divergence symmetry" method,

this includes a mixture Gaussian and Lorentzian broadening of the peak shape, consistent with our instrumental resolution. Based on the refined parameters, a physical representation of the crystal structure is created by using VESTA.

3. Results & Discussion:

Structural heterogeneity: We have first performed structural analysis of as-synthesized doped-PNCs to trace the origin of their enhanced optical properties and improved ambient stability. Full-Survey and High-resolution XPS spectra of doped PNCs for Pb 4f yield two distinct gaussian-shaped peaks due to spin-orbit coupling of 4f-orbital, as shown in Figure S1-2. The Pb 4f peaks in XPS spectrum of Ni:Co:PNC and Co:PNC appears at 142.7 eV ($4f_{5/2}$) and 137.8 eV ($4f_{7/2}$), nearly at same position of the undoped- $CsPbBr_3$.[42] The Pb 4f peaks of Ni:PNC are shifted to higher binding energy, that is, at 143.4 eV ($4f_{5/2}$) and 138.6 eV ($4f_{7/2}$). The spin-obit splitting of Pb(II) for both remains same, 4.9 eV. XPS peak positions of core-level spectra are vastly affected by chemical environment (surrounding electron-cloud) of that element. It therefore suggests that Ni(II) greatly impacts chemical environment around Pb(II) in nanocrystal.[43] The Ni-doping might enhance the chemical bonding of Pb with neighboring bromide ion causing peak in higher-binding energy.[44] Such effect is minimal for doping of Co(II) ion. Interestingly, insignificant shifting of Pb 4f peaks in Ni:Co:PNC compared to that of Co:PNC suggests a similar environment of Pb in both the combinations. It is possible that the combination of Co and Ni doping in Ni:Co:PNC may not affect the Pb-Br bond but may affect the overall structure, i.e. distortion of overall lattice structure. Notably, the XPS spectra of Ni(II) for Ni:Co:PNC greatly resembles with that for Ni:PNC (Figure S3).

Thereafter, we have analyzed Energy-dispersive X-ray spectra (EDS) of Ni:PNC, Ni:Co:PNC and Co:PNC (Figure S4) to estimate the dopant concentration in metal-doped perovskite nanocrystals. Elemental ratio of Cs:Pb:Br of metal-doped PNCs is found to be 1:1:3, confirming $CsPbBr_3$ composition. The atomic percentage of Ni(II) in Ni:PNC and Ni:Co:PNC are 2.3 and 0.8 respectively, whereas that of Co(II) in Ni:Co:PNC and Co:PNC are 1.0, and 2.4 respectively.

Hence, doping of about 2% metal ions in PNCs creates a strong impact in the structural heterogeneity.

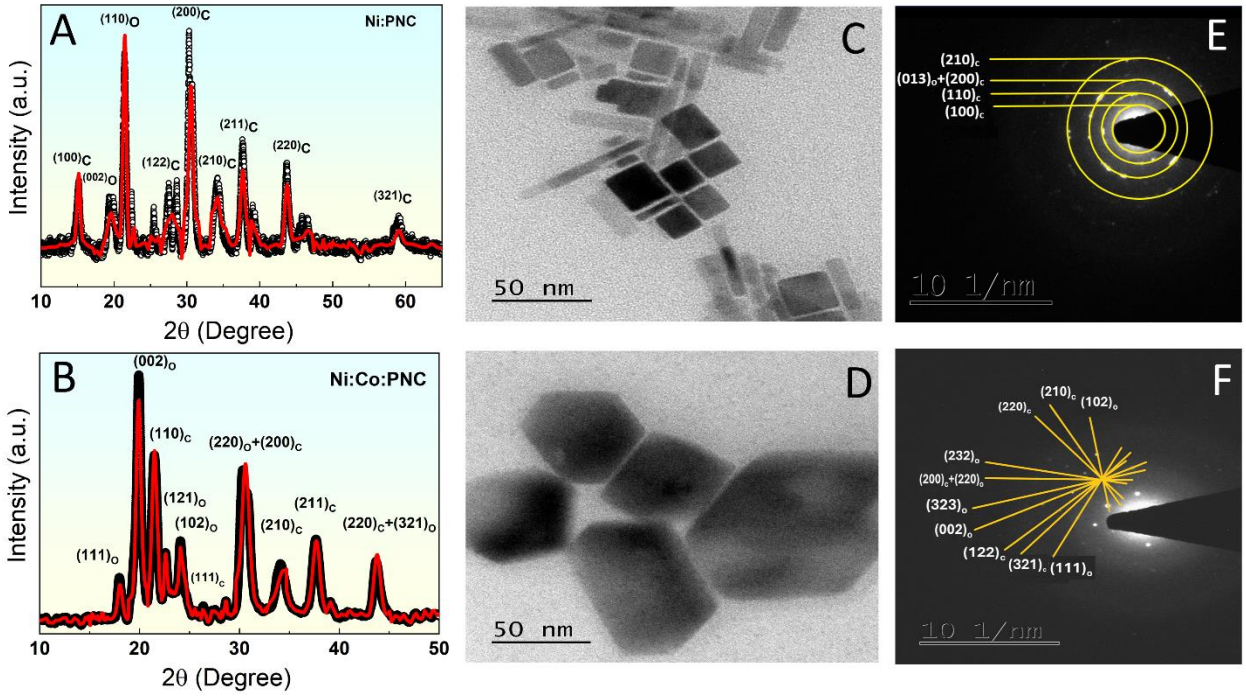

Figure 1: Rietveld refinement of the X-ray diffraction pattern of- **[A]** Ni:PNC and **[B]** Ni:Co:PNC. The data are shown as circles, and the result of the refinement as a solid line (red). We have used orthorhombic phase (space group: Pnma, No. 62) of $CsPbBr_3$ and added cubic phase (space group: Pm-3m, No. 221). **[C-D]** TEM Images of Ni:PNC and Ni:Co:PNC. respectively. **[E-F]** TEM-FFT pattern of Ni:PNC and Ni:Co:PNC. respectively.

X-ray diffraction (XRD) studies have been performed to resolve the facet engineering through metal-doping of perovskite nanocrystals. Our careful Rietveld refinement demonstrates that doped perovskite nanocrystals exist in two phases - orthorhombic and cubic phases. [45,46] The Rietveld-refined XRD patterns of Ni:PNC and Ni:Co:PNC are shown in Figure 1A-B. The percentage of orthorhombic and cubic phase vastly varies with doping. Unprecedentedly, facet engineering through metal-doping has been noticed with observation of {100} facet only in Ni:PNC. Emergence of facet {111} for Ni:Co:PNC signals its significant structural change in comparison to that of Ni:PNC. The displacement of Cs-ion in orthorhombic structure

(maintaining same space-group) in Ni:Co:PNC compared to that of Ni:PNC plays the crucial role for such facet engineering. Subtle change in position of Cs ions in Ni:Co:PNC nanocrystal in comparison to that of Ni:PNC nanocrystal has been observed, while negligible change of Br and no change of Pb atom is noticed (Figure S5). Cs-atom in Ni:Co:PNC systematically shifts towards the surface of the orthorhombic structure which forms an irregular hexagon (Figure S5A).[47] However, the Cs ions get displaced in one direction for Ni:PNC, therefore, does not construct such systematic dodecahedron structure (Figure S5B). Eventually, the one-directional movement of Cs-atom in Ni:PNC suggests the possibility of spatial inversion symmetry breakings. We have imaged the doped perovskite nanocrystals- Ni:PNC and Ni:Co:PNC by using transmission electron microscopy (TEM) to further support such changes in crystal structure.

Figure 1C shows typical cubic (15.8 nm ± 4.1) and nanorod (width: 9.1 nm ± 2.4; length: 49.2 nm± 18.2) structures of Ni:PNC while Figure 1D captures the elongated hexagon (43.0 nm ± 16.3). In addition to that, we have also observed a perfect hexagon structure for Ni:Co:PNC (Figure S6). Lattice spacing observed for Ni:PNC is 0.55 nm whereas that for Ni:Co:PNC is 0.83 nm (Figure S6). By analyzing the reciprocal crystal point in the TEM images (Figure 1D-E), we have measured the d-spacing values and associated them with specific {hkl} planes. Facets {100}, {110} and {200} of Ni:PNC correspond to the family of planes of cubic $CsPbBr_3$. Whereas, presence of facets {111}, {002}, and {211} signifies predominant orthorhombic structure of Ni:Co:PNC. Our refined crystallographic analysis, combined with the creation of a physical structure based on the refinement parameters, reveals an intriguing pattern within the orthorhombic phase. The absence of atoms at the corners and the resulting formation of a trapezo-rhombic dodecahedral-like structure (elongated dodecahedron) closely corresponds to

the observed hexagonal pattern observed in TEM image. Structural analysis using Rietveld Refinement suggests that the ratio of total integrated intensities between orthorhombic and cubic phase for Ni:Co:PNC is 55:45, whereas that for Ni: PNC becomes 25:75. Moreover, plane {100} of Ni:PNC cuts four Cs(I) ion and a Bromide ion whereas plane {111} of Ni:Co:PNC consists of two Pb(II) ions and one bromide ion (Figure 2). By analyzing the reciprocal crystal point in the TEM image, we measured the d-spacing values and associated them with specific hkl planes. The consistency observed between our calculated d-spacing values and the refined crystallographic parameters validated the accuracy of our approach. The agreement between the predicted planes from the TEM-FFT pattern analysis and the refinement results from XRD contribute to a deeper understanding of the structural modifications induced by dopants- Ni(II) and Co (II) in the $CsPbBr_3$ lattice.

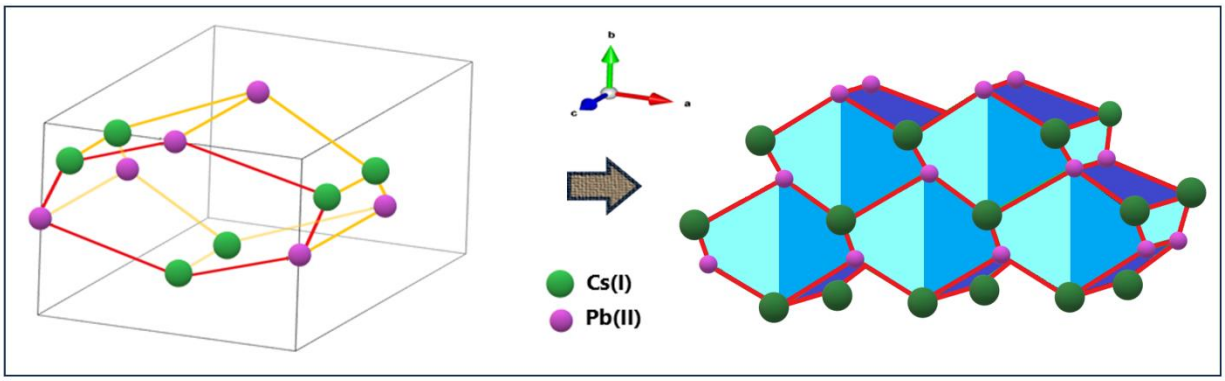

Figure 2: Front surface on ab plane (solid red lines) of Ni:Co:PNC. Addition of adjacent trapezoid (solid yellow line) results in formation of dodecahedron structure. Ni:Co:PNC crystal lattice having Cs(I) and Pb(II) ions only. On the front surface of ab plane by connecting Pb-Cs-Pb-Cs-Pb-Cs-Pb, front hexagonal is first sketched and then extending the whole structure in all direction to elongated dodecahedron.

Enhanced Photoluminescence and Ambient Stability: Ni/Co-doped Cesium Lead Bromide Perovskite Nanocrystals- Ni:PNC, Co:PNC and Ni:Co:PNC dispersed in hexane more-or-less

retains the green-emissive features of pristine PNC. The emission peak positions (λ_{max}) are centered at 518 nm (fwhm = 18 nm) with a band gap of 2.30 eV for Ni:PNC (Figure S7-8). However, the emission peak of Ni:Co:PNC gets blue-shifted to 515 nm (fwhm = 19 nm) with a band gap of 2.32 eV. The photoluminescence quantum yield (PLQY) of Ni:Co:PNC is measured to be 0.70 whereas that of Co:PNC and Ni:PNC are relatively low, 0.54 and 0.33 respectively. The augmented photoluminescence properties of doped-PNCs may be accounted for by invoking either Spin-Orbit Coupling (quantum hoping) or structural (facet) engineering.[43] We have found that Ni:PNC and Ni:Co:PNC are relatively more stable than Co:PNC (Figure S9). The stability of Ni:PNC is in agreement with reported results.[31,44] Crystal stiffening caused by smaller ionic radii of Ni(II) ion has been attributed to the improved stability of Ni:PNC as well. The average photoluminescence lifetimes, τ_{avg} of Ni:PNC, Ni:Co:PNC in toluene are 4.68 ns, 5.47 ns respectively, whereas that of Co:PNC is relatively low, 2.57 ns (Table S1, Figure S7B & S10). It can be mentioned that toluene acts as a photoluminescent quencher for doped-PNC. Hence, this photophysical study serves as a reference point for energy transfer studies in toluene medium.

Crystal Facet-directed Energy Transfer to Rhodamine B: Energy transfer studies between organic fluorophores are often manipulated by regulating the binding affinity between acceptor and donor moieties.[48,49] However, understanding of energy transfer process involving nanocrystal and organic molecules is at a very early stage. Recently, it has been suggested that pendant groups of acceptor molecules can also regulate their binding affinity toward perovskite nanocrystals.[36] An obvious question thus arises– how does electronegative atom (e.g. iodine, chlorine) of acceptor molecule influence its binding affinity to perovskite nanocrystal? The role

of crystal facets in doped-PNCs cannot be ignored as it has also been shown that facet {100} $FAPbI_3$ strongly interacts with highly polar water molecules.[9]

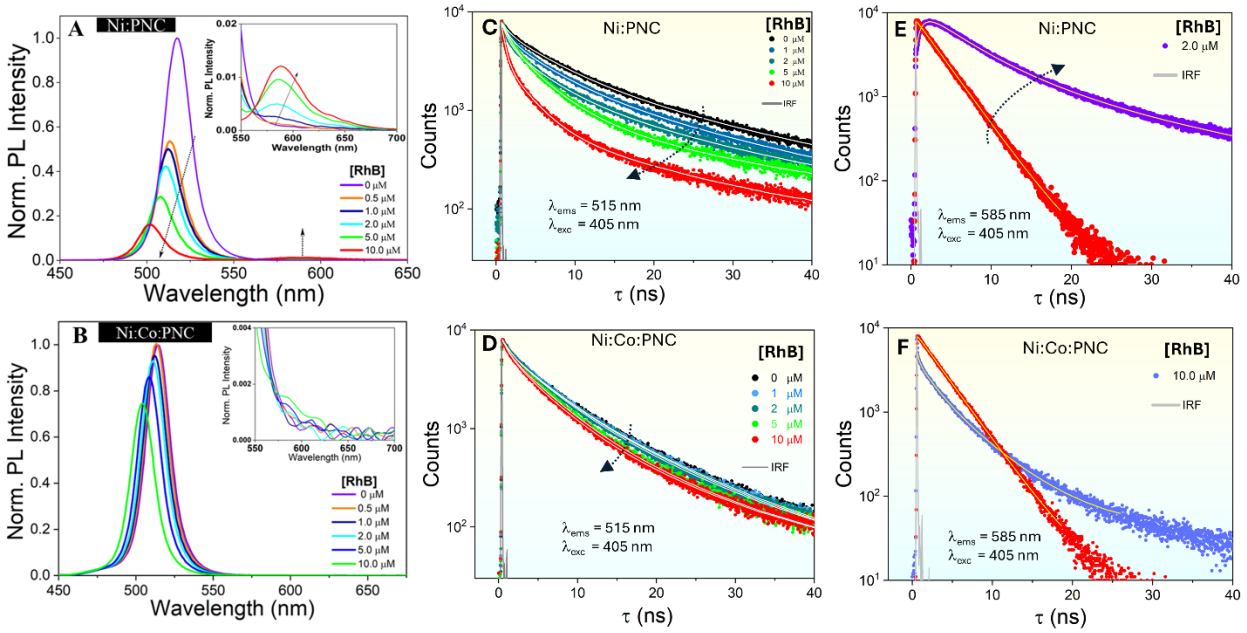

Figure 3: Photoluminescence quenching of Donors– [A] Ni:PNC and [B] Ni:Co:PNC with successive addition of acceptor, Rhodamine B. *Inset:* Modulation of emission properties of acceptor. Time-resolved photoluminescence decays at λ_{ems} = 515 nm of-. [C] Ni:PNC and [D] Ni:Co:PNC highlighting faster kinetics upon gradual addition of rhodamine B. **[E-F]** Time-resolved photoluminescence decays of acceptor (λ_{ems} = 585 nm) for Ni:PNC-RhB pair and Ni:Co:PNC-RhB pair respectively. Instrument response function (IRF) at λ_{exc} = 405 nm represented in grey line.

To interrogate the efficiency of energy transfer, we have measured steady-state and time-resolved emission spectra of donors - Ni:PNC, Ni:Co:PNC and Co:PNC in presence and absence of acceptor, Rhodamine B (Figure 3A-B and Figures S11-12). The photoluminescence of donors undergoes gradual quenching with addition of Rhodamine B (0–10 μM). However, the photoluminescence quenching for Ni:PNC is relatively sharp than that of Ni:Co:PNC (Figure 3A-B). Interestingly, concurrent emission of acceptor is pronounced for Ni:PNC–RhB pair (Inset, Figure 3A) whereas hardly any emission originates from acceptor for Ni:Co:PNC–RhB pair (Inset, Figure 3B). Isoemissive point that appears at 560 nm is suggestive of existence of

two emissive species— Ni:PNC* and [Ni:PNC-RhB*] in equilibrium. A hypsochromic shift in photoluminescence spectra of M:PNC is due to presence of chloride ion in commercially available Rhodamine B (Empirical formula: $C_{28}H_{31}ClN_2O_3$).

Synchronicity between decrease in donor emission and concurrent increase in acceptor emission is commonly observed for organic donor-acceptor systems. It seems that such synchronicity is missing for doped PNC-RhB system as evident by low concurrent emission of fluorophore and significant decrease in emission of doped PNCs. To account for this observation, we have drawn its similarity with widely reported interactions of metal nanoparticles (such as Au, Ag nanoparticles) with organic fluorophores. The cause of significant photoluminescence quenching of doped PNC can thus be attributed to the specific interaction (such as adsorption, electron transfer) of Rhodamine B with its surface. Moreover, to shed a light on the molecular characteristics of Rhodamine B in solvent toluene, we have performed photophysical studies of Rhodamine B alone in toluene (Figure S13). It resolves that RhB starts forming molecular aggregates at its increased concentration signaled by decrease in its fluorescence lifetime. Such heterogeneity is thus expected to exhibit concentration-dependent energy transfer dynamics for M:PNC-RhB system.

Time-resolved photoluminescence studies of D-A pairs are in direct conformity with steady-state photoluminescence studies. TRPL decays of Ni:PNC–RhB and Ni:Co:PNC–RhB pairs at 515 nm (λ_{exc} = 405 nm) with gradual addition of acceptor (0–10 μM) become faster (Figure 3C-D) and associated decay parameters are tabulated in Table S2-S3. However, the decrease in τ_{avg} for Ni:PNC–RhB is 83% whereas that for Ni:Co:PNC–RhB remains merely 20%. It is evident that the emission of RhB originates from the excitation of doped-PNCs and direct energy transfer from perovskite nanocrystals to organic fluorophore yields a singlet excited state of acceptor.

Involvement of Triplet-Triplet (T-T) annihilation has been negated because the formation of singlet excited state of acceptor, Rhodamine B is dependent on excited state decay of donor, doped-PNC. To quantify the rate of energy transfer for Ni:PNC–RhB pair, we have recorded fluorescence decay of Rhodamine B at 585 nm (λ_{exc} = 405 nm) in presence and absence of donor, Ni:PNC (Figure 3E). Emergence of rise-time in fluorescence decay of Rhodamine B confirms the energy transfer from Ni:PNC (Table S4). However, there is no rise-time noticed for Ni:Co:PNC–RhB pair even at 10 μM concentration of Rhodamine B (Figure 3F & Table S5). Similarly, we have also performed energy transfer studies for Co:PNC–RhB pair (Figure S14 & Table S6-7).

To further substantiate the light-harvesting abilities of doped Ni:PNC-RhB system, we have investigated their energy transfer dynamics in thin-film as well. The concentrations of acceptor, RhB have been kept relatively low to avoid unwarranted molecular aggregation. The photoluminescence of Ni:PNC drops dramatically even at 0.5 μM of Rhodamine B. Thereafter, it follows a common trend observed for energy transfer— decrease in Ni:PNC emission with concurrent increase in RhB emission (Figure 4A). TRPL decays of Ni:PNC–RhB in thin films at 512 nm (λ_{exc} = 405 nm) with gradual addition of acceptor (0–10 μM) become faster (Figure 4B, Table S8). Rise-time in fluorescence decay of RhB again bolsters the efficient energy transfer from Ni:PNC (Figure 4C, Table S9). Rate of energy transfer in thin film is much faster than that in solution (Table 1). It therefore suggests that Rhodamine B resides in close-proximity with Ni:PNC in thin-films owing to arrested diffusion.

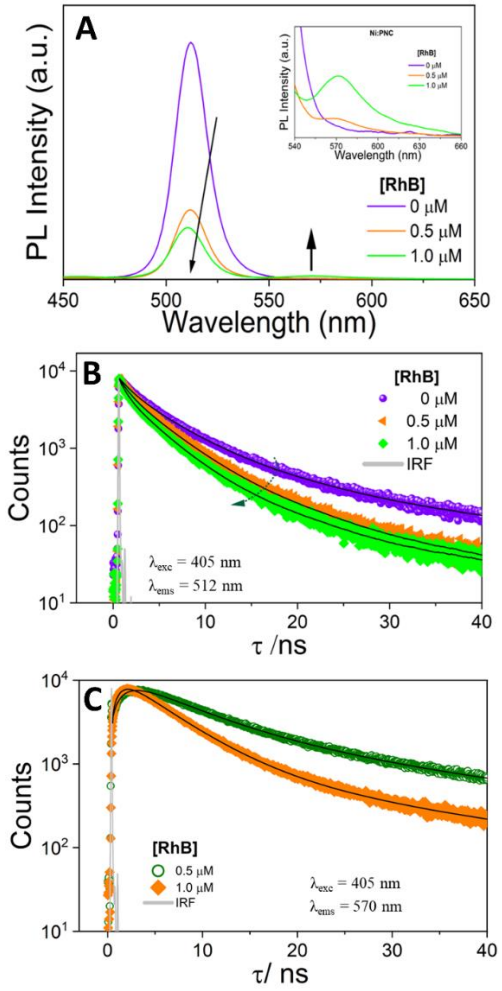

Figure 4: [A] Photoluminescence spectra of Ni:PNC in presence of RhB in thin-films. Inset: Concomitant increase in fluorescence of RhB. **[B]** Time-resolved photoluminescence decays at λ_{ems} = 512 nm at varied concentration of rhodamine B in thin films. **[C]** Time-resolved photoluminescence decays of acceptor, RhB (λ_{ems} = 570 nm) at its two different concentrations in thin films for Ni:PNC-RhB pair.

Resonance Energy Transfer (RET) is popularly known as fluorescence resonance energy transfer (FRET) that involves a nonradiative energy transfer from an electronic excited state of a donor molecule (D*) to the ground state of an acceptor molecule. [48,49] Förster theory for energy transfer processes assumes dipole-dipole interactions and predicts that the rate of RET follows a $1/R^6$-type distance dependence, where R is the center-to-center distance between D and A. However, a significant deviation from $1/R^6$ dependence is observed for donor-acceptor systems with increased asphericity. Bagchi and coworkers have formulated that rate of RET follows $1/R^4$

dependence for nanoparticle-fluorophore systems.[50,51] To quantify the energy transfer for M:PNC-Rhodamine systems rise time of acceptor is being exploited. The excited state concentration of the acceptor, $A^*(t)$, generated via FRET, is proportional to the time-resolved fluorescence intensity of donor $I_{DA\ (t)}$ in presence of acceptor. Moreover, this donor-acceptor system is relatively homogenous and random solution with no excluded volume. Considering the cubic and elongated dodecahedron structures for doped-PNCs, we have quantified the rate of energy transfer and efficiency of energy transfer (E_{FRET}) by using formalism of $1/R^4$ dependence for FRET.

$$k_{FRET} = \frac{1}{{\tau_A}^{rise}} = \frac{1}{\tau_D}\left(\frac{R_0}{R_{DA}}\right)^4 \text{ ---------- (1) for D-A pair with acceptor's rise-time}$$

$$k'_{FRET} = \left(\frac{1}{\tau_{DA}} - \frac{1}{\tau_D}\right) = \frac{1}{\tau_D}\left(\frac{R_0}{R_{DA}}\right)^4 \text{ ---------- (2) for D-A pair without acceptor's rise-time}$$

$$E_{FRET} = \frac{{R_0}^4}{{R_0}^4 + {R_{DA}}^4}$$

Where ${\tau_A}^{rise}$ is the rise-time component of acceptor, τ_{DA} is the donor's lifetime with acceptor, τ_D is the donor's lifetime (without acceptor), R_0 is the Förster distance, and R_{DA} is the D−A distance.

Table 1 & Table S10 summarize all the quintessential parameters associated with FRET efficiency, $E_{FRET.}$ FRET efficiency for M:PNC-dye systems. FRET efficiency for Ni:PNC-RhB pair is estimated to be 94% (Equation 1). Quantified FRET efficiency by using Equation 2 for Ni:PNC-RhB is 82% whereas for Ni:Co:PNC-RhB pair it remains just 21%. And FRET efficiency is found to be greatly influenced by the distance between donor and acceptor, R_{DA}. The rate of energy transfer of D-A pair is inversely related with photoluminescence quantum yield of donor. Moreover, the spectral overlap integral, J(λ) is hardly impacting either k_{FRET} .or k'_{FRET} (Table 1, & Table S8).

Table 1: Efficiency of Energy Transfer and associated parameters for different Donor-Acceptor pairs.

	Donor	[RhB] (μM)	PLQY (Donor)	$< \tau_D >$ (ns)	J(λ) ($M^{-1}cm^{-1}nm^4$)	τ_A^{rise} (ns)	k_{FRET} (10^9 s^{-1})	R_0 (Å)	R_{DA} (Å)	E_{FRET} (%)
Toluene	Ni:PNC	2	0.32	4.68	2.10	0.90	1.11	30.49	20.19	**84**
		10				0.31	3.22		15.47	**94**
	Co:PNC	10	0.44	2.57	2.09	0.75	1.33	31.89	23.45	**77**
	Ni:Co:PNC	10	0.62	5.47	1.92	–	0.05*	33.53	46.36	**21**
Thin film	Ni:PNC	0.5	—	5.05	1.87	1.48	0.67	$k_{FRET} = \frac{1}{\tau_A^{rise}}$ for D-A pair with appearance of rise-time, *$k'_{FRET} = \left(\frac{1}{\tau_{DA}} - \frac{1}{\tau_D}\right)$ for D-A pair with non-appearance of rise time.		
		1.0	—	5.05		0.93	1.07			

It therefore raises a very pertinent question – what is the reason for variation of R_{DA}? Hence, to provide a rationale, we have performed the binding studies of Rhodamine B with metal-doped PNCs. Double-reciprocal plots have been constructed to measure the apparent association constants (K_{app}) of Rhodamine B with metal-doped PNCs (Figure S15). The estimated K_{app} value for Ni:PNC–RhB pair is relatively high, 10.2×10^5 M^{-1} whereas that for Ni:Co:PNC–RhB pair is quite low, 0.38×10^5 M^{-1}. It therefore suggests preferential binding interactions of Rhodamine B with metal-doped PNCs. Moreover, Figure 5 highlights the pivotal role of association constant (K_{app}) on regulating the energy transfer dynamics of M:PNC-RhB pairs.

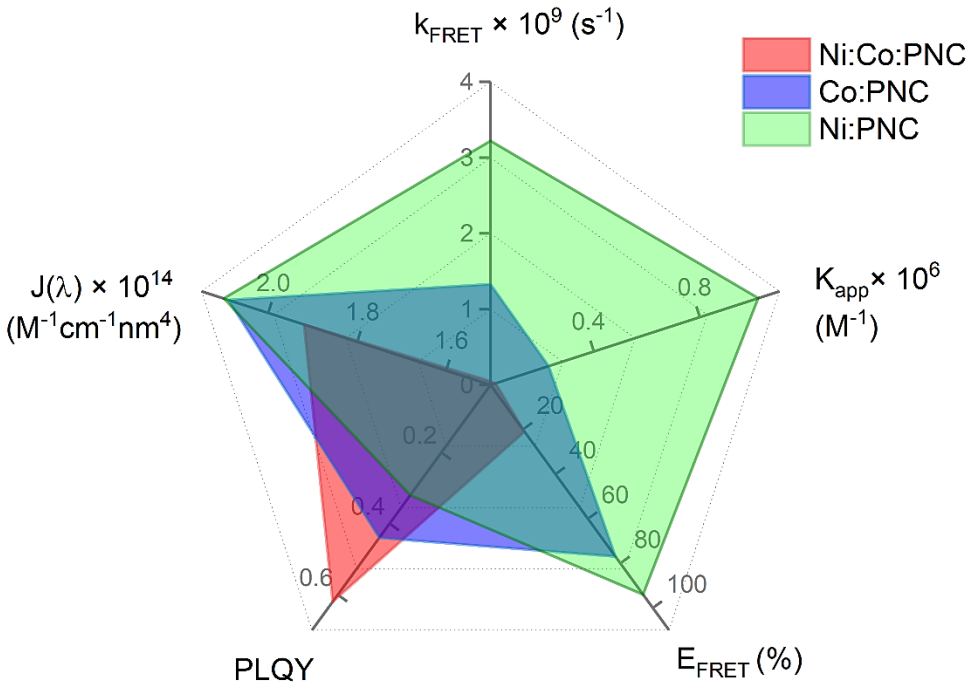

Figure 5: A radar plot highlighting dependence of rate of energy transfer, k_{FRET} and efficiency of energy transfer, E_{FRET} on spectral overlap integral, J(λ), PLQY and apparent binding constant (K_{app}) for M:PNC-RhB pairs.

Such a huge variation in binding constant cannot be obtained without either compositional variation of crystal facets or preferential interaction of oleylamine/oleic acid with facets. The basis of this hypothesis stems from the recent observation that cyclohexamine gets preferentially absorbed at {111} facet of $FaPbI_3$ perovskite. However, accurate quantification of surface composition or stoichiometry of facets {100} and {111} is quite difficult, hence, we have analyzed structural features through Rietveld Refinement. Hence, facet {100} offers a conducive chemical environment for Rhodamine B due to presence of number of cesium ions and thus fosters dipole-dipole interaction such as FRET.[37,52] However, presence of Pb(II) in facet {111} enforces specific adhesion with oleyamine due to chelation/metal-ligand type of interactions, hence, block the access of Rhodamine B to Ni:Co:PNC nanocrystal.[53,54]

4. Conclusion:

We have demonstrated facet-engineering of $CsPbBr_3$ perovskite nanocrystals with doping of trace-amounts of Nickel (II) and Cobalt (II) ions. Ni:PNC retains regular cubic and rod-like structures, whereas Ni:Co:PNC evolves to irregular dodecahedron structure. Doping of Nickel ion in $CsPBBr_3$ crystal lattice renders crystal stiffening for Ni:PNC, while it distorts the crystal structure of Ni:Co:PNC by repositioning of atoms in lattice. The ambient stability and photoluminescence property gets significantly augmented for Ni:Co:PNC in comparison to that of Ni:PNC. We have identified that mode of Energy transfer remains Foster Resonance Energy Transfer. Ni:PNC dominated with facet {100} records impressive FRET efficiency for Rhodamine B, whereas Ni:Co:PNC dominated with facet {111} shows very poor efficiency to the same acceptor. Observation of regular and irregular structures with crystallographic termination and role of surface composition of facet {100} of metal-doped PNCs have been rationalized through structural analysis using Rietveld refinement. The size of metal-doped PNCs is hardly playing any role on its energy transfer dynamics with organic fluorophore, RhB.

■ Supporting Information:

Methods section, estimation of FRET, XPS characterization results, Rietveld Refinement analysis, HRTEM images, Apparent Binding Constants. Additional characterization data including steady state and time-resolved fluorescence measurements.

■ Conflict of Interests:

The authors declare no competing financial interest.

■ Author Contributions:

D.P. designed the research; S.P. performed research; S.P., and D.P. analyzed data; G.R. and T.B. performed Rietveld Refinement, and D.P. wrote the article.

■ Acknowledgements:

The authors greatly acknowledge Rajiv Gandhi Institute of Petroleum Technology for financial support (Project No. IG-2104). S.P. and G.R. thank RGIPT for Institute fellowship respectively. The authors acknowledge Central Instrumentation Facilities at RGIPT, the Advanced Imaging Center (AIC) at IIT Kanpur for instrumentation facilities.

5. References

1 A. Dey, J. Ye, A. De, E. Debroye, S. K. Ha, E. Bladt, A. S. Kshirsagar, Z. Wang, J. Yin, Y. Wang, L. N. Quan, et al., State of the Art and Prospects for Halide Perovskite Nanocrystals, *ACS Nano*, 2021, **15**, 10775–10981.

2 A. K. Jena, A. Kulkarni and T. Miyasaka, Halide Perovskite Photovoltaics: Background, Status, and Future Prospects, *Chem. Rev.*, 2019, **119**, 3036–3103.

3 Y. Fu, H. Zhu, J. Chen, M. P. Hautzinger, X.-Y. Zhu and S. Jin, Metal halide perovskite nanostructures for optoelectronic applications and the study of physical properties, *Nat. Rev. Mater.*, 2019, **4**, 169–188.

4 H. Huang, D. Verhaeghe, B. Weng, B. Ghosh, H. Zhang, J. Hofkens, J. A. Steele and M. B. J. Roeffaers, Metal Halide Perovskite Based Heterojunction Photocatalysts, *Angew. Chemie Int. Ed.*, 2022, **61**, e202203261.

5 Q. A. Akkerman, G. Rainò, M. V. Kovalenko and L. Manna, Genesis, challenges and opportunities for colloidal lead halide perovskite nanocrystals, *Nat. Mater.*, 2018, **17**, 394–405.

6 N. Fiuza-Maneiro, K. Sun, I. López-Fernández, S. Gómez-Graña, P. Müller-Buschbaum and L. Polavarapu, Ligand Chemistry of Inorganic Lead Halide Perovskite Nanocrystals, *ACS Energy Lett.*, 2023, **8**, 1152–1191.

7 J. De Roo, M. Ibáñez, P. Geiregat, G. Nedelcu, W. Walravens, J. Maes, J. C. Martins, I. Van Driessche, M. V. Kovalenko and Z. Hens, Highly Dynamic Ligand Binding and Light Absorption Coefficient of Cesium Lead Bromide Perovskite Nanocrystals, *ACS Nano*, 2016, **10**, 2071–2081.

8 Y. Zhang, T. D. Siegler, C. J. Thomas, M. K. Abney, T. Shah, A. De Gorostiza, R. M.

Greene and B. A. Korgel, A “Tips and Tricks” Practical Guide to the Synthesis of Metal Halide Perovskite Nanocrystals, *Chem. Mater.*, 2020, **32**, 5410–5423.

9 C. Ma, F. T. Eickemeyer, S.-H. Lee, D.-H. Kang, S. J. Kwon, M. Grätzel and N.-G. Park, Unveiling facet-dependent degradation and facet engineering for stable perovskite solar cells, *Science*, 2023, **379**, 173–178.

10 J.-P. Ma, J.-K. Chen, J. Yin, B.-B. Zhang, Q. Zhao, Y. Kuroiwa, C. Moriyoshi, L. Hu, O. M. Bakr, O. F. Mohammed and H.-T. Sun, Doping Induces Structural Phase Transitions in All-Inorganic Lead Halide Perovskite Nanocrystals, *ACS Mater. Lett.*, 2020, **2**, 367–375.

11 G. H. Ahmed, Y. Liu, I. Bravić, X. Ng, I. Heckelmann, P. Narayanan, M. S. Fernández, B. Monserrat, D. N. Congreve and S. Feldmann, Luminescence Enhancement Due to Symmetry Breaking in Doped Halide Perovskite Nanocrystals, *J. Am. Chem. Soc.*, 2022, **144**, 15862–15870.

12 N. Pradhan, Tips and Twists in Making High Photoluminescence Quantum Yield Perovskite Nanocrystals, *ACS Energy Lett.*, 2019, **4**, 1634–1638.

13 S. Das, A. De and A. Samanta, Ambient Condition Mg2+ Doping Producing Highly Luminescent Green-and Violet-Emitting Perovskite Nanocrystals with Reduced Toxicity and Enhanced Stability, *J. Phys. Chem. Lett.*, 2020, **11**, 1178–1188.

14 Z. He, X. Liang and W. Xiang, High-efficiency Ca2+ doping all-inorganic nanocrystals (CsPbBr3 and CsPbBr1I2) encapsulated in a superhydrophobic aerogel inorganic matrix for white light-emitting diodes, *Chem. Eng. J.*, 2022, **427**, 130964.

15 J.-K. Chen, J.-P. Ma, S.-Q. Guo, Y.-M. Chen, Q. Zhao, B.-B. Zhang, Z.-Y. Li, Y. Zhou, J. Hou, Y. Kuroiwa, C. Moriyoshi, O. M. Bakr, J. Zhang and H.-T. Sun, High-Efficiency Violet-Emitting All-Inorganic Perovskite Nanocrystals Enabled by Alkaline-Earth Metal

Passivation, *Chem. Mater.*, 2019, **31**, 3974–3983.

16 N. Mondal, A. De and A. Samanta, Achieving Near-Unity Photoluminescence Efficiency for Blue-Violet-Emitting Perovskite Nanocrystals, *ACS Energy Lett.*, , DOI:10.1021/acsenergylett.8b01909.

17 G. H. Ahmed, Y. Liu, I. Bravić, X. Ng, I. Heckelmann, P. Narayanan, M. S. Fernández, B. Monserrat, D. N. Congreve and S. Feldmann, Luminescence Enhancement Due to Symmetry Breaking in Doped Halide Perovskite Nanocrystals, *J. Am. Chem. Soc.*, 2022, **144**, 15862–15870.

18 A. Garai, E. K. Vishnu, S. Banerjee, A. A. K. Nair, S. Bera, K. G. Thomas and N. Pradhan, Vertex-Oriented Cube-Connected Pattern in CsPbBr 3 Perovskite Nanorods and Their Optical Properties: An Ensemble to Single-Particle Study , *J. Am. Chem. Soc.*, 2023, **145**, 13989–13999.

19 M. K. Gangishetty, S. N. Sanders and D. N. Congreve, Mn 2+ Doping Enhances the Brightness, Efficiency, and Stability of Bulk Perovskite Light-Emitting Diodes, *ACS Photonics*, 2019, **6**, 1111–1117.

20 S. Seth, T. Ahmed, A. De and A. Samanta, Tackling the Defects, Stability, and Photoluminescence of CsPbX 3 Perovskite Nanocrystals, *ACS Energy Lett.*, 2019, **4**, 1610–1618.

21 H. B. Gray, *Nat. Chem.*, 2009, 1, 7.

22 H. Huang, B. Pradhan, J. Hofkens, M. B. J. Roeffaers and J. A. Steele, Solar-Driven Metal Halide Perovskite Photocatalysis: Design, Stability, and Performance, *ACS Energy Lett.*, 2020, **5**, 1107–1123.

23 S. Shyamal, S. K. Dutta and N. Pradhan, Doping Iron in CsPbBr 3 Perovskite

Nanocrystals for Efficient and Product Selective CO 2 Reduction, *J. Phys. Chem. Lett.*, 2019, **10**, 7965–7969.

24 M. Gao, J. Fan, X. Li, Q. Wang, D. Li, J. Feng and X. Duan, A Carbon-Negative Hydrogen Production Strategy: CO2 Selective Capture with H 2 Production, *Angew. Chemie Int. Ed.*, 2023, **62**, e202216527..

25 A. Manna, T. K. Dinda, S. Ghosh and P. Mal, CsPbBr 3 in the Activation of the C–Br Bond of CBrX 3 (X = Cl, Br) under Sunlight, *Chem. Mater.*, 2023, **35**, 628–637.

26 P. V. Kamat, Semiconductor Surface Chemistry as Holy Grail in Photocatalysis and Photovoltaics, *Acc. Chem. Res.*, 2017, **50**, 527–531.

27 P. Zhang, X. Yang, S. Du, L. Yin, J. Wang, P. Liu and W. Hou, Insight into the Crystal Facet Effect of {101} and {100} Facets of CeVO4 in the Photochemical Property and Photocatalysis, *J. Phys. Chem. Lett.*, 2022, **13**, 10432–10438.

28 S. Shyamal, S. K. Dutta, T. Das, S. Sen, S. Chakraborty and N. Pradhan, Facets and Defects in Perovskite Nanocrystals for Photocatalytic CO2Reduction, *J. Phys. Chem. Lett.*, 2020, **11**, 3608–3614.

29 Y.-F. Xu, M.-Z. Yang, H.-Y. Chen, J.-F. Liao, X.-D. Wang and D.-B. Kuang, Enhanced Solar-Driven Gaseous CO 2 Conversion by CsPbBr 3 Nanocrystal/Pd Nanosheet Schottky-Junction Photocatalyst, *ACS Appl. Energy Mater.*, 2018, **1**, 5083–5089.

30 C. Bi, S. Wang, Q. Li, S. V. Kershaw, J. Tian and A. L. Rogach, Thermally Stable Copper(II)-Doped Cesium Lead Halide Perovskite Quantum Dots with Strong Blue Emission, *J. Phys. Chem. Lett.*, 2019, **10**, 943–952.

31 R. K. Behera, A. Dutta, D. Ghosh, S. Bera, S. Bhattacharyya and N. Pradhan, Doping the Smallest Shannon Radii Transition Metal Ion Ni(II) for Stabilizing α-CsPbI 3 Perovskite

Nanocrystals, *J. Phys. Chem. Lett.*, 2019, **10**, 7916–7921.

32 Y. Barak, I. Meir, J. Dehnel, F. Horani, D. R. Gamelin, A. Shapiro and E. Lifshitz, Uncovering the Influence of Ni2+ Doping in Lead-Halide Perovskite Nanocrystals Using Optically Detected Magnetic Resonance Spectroscopy, *Chem. Mater.*, 2022, **34**, 1686–1698.

33 H. Choi, R. Nicolaescu, S. Paek, J. Ko and P. V. Kamat, Supersensitization of CdS Quantum Dots with a Near-Infrared Organic Dye: Toward the Design of Panchromatic Hybrid-Sensitized Solar Cells, *ACS Nano*, 2011, **5**, 9238–9245.

34 P. Maity, J. Dana and H. N. Ghosh, Multiple Charge Transfer Dynamics in Colloidal CsPbBr3 Perovskite Quantum Dots Sensitized Molecular Adsorbate, *J. Phys. Chem. C*, 2016, **120**, 18348–18354.

35 J. T. Dubose and P. V. Kamat, Directing energy transfer in halide perovskite-chromophore hybrid assemblies, *J. Am. Chem. Soc.*, 2021, **143**, 19214–19223.

36 J. T. DuBose and P. V. Kamat, How Pendant Groups Dictate Energy and Electron Transfer in Perovskite–Rhodamine Light Harvesting Assemblies, *J. Am. Chem. Soc.*, 2023, **145**, 4601–4612.

37 P. Aggarwal, A. Halder, Neelakshi, R. Ramapanicker and V. Govind Rao, Energy Funneling from Water-Dispersed Perovskites to Chromophores, *ACS Energy Lett.*, 2023, **8**, 1520–1528.

38 N. Pradhan, Why Do Perovskite Nanocrystals Form Nanocubes and How Can Their Facets Be Tuned? A Perspective from Synthetic Prospects, *ACS Energy Lett.*, 2021, **6**, 92–99.

39 A. Boulesbaa, Z. Huang, D. Wu and T. Lian, Competition between energy and electron

transfer from CdSe QDs to adsorbed rhodamine B, *J. Phys. Chem. C*, 2010, **114**, 962–969.

40 T. Basu, V. V. R. Kishore, S. Gohil, K. Singh, N. Mohapatra, S. Bhattacharjee, B. Gonde, N. P. Lalla, P. Mahadevan, S. Ghosh and E. V. Sampathkumaran, Displacive-type ferroelectricity from magnetic correlations within spin-chain, *Sci. Rep.*, 2014, **4**, 1–6.

41 K. Momma and F. Izumi, VESTA 3 for three-dimensional visualization of crystal, volumetric and morphology data, *J. Appl. Crystallogr.*, 2011, **44**, 1272–1276.

42 T. Ahmed, S. Seth and A. Samanta, Boosting the Photoluminescence of CsPbX 3 (X = Cl, Br, I) Perovskite Nanocrystals Covering a Wide Wavelength Range by Postsynthetic Treatment with Tetrafluoroborate Salts, *Chem. Mater.*, 2018, **30**, 3633–3637.

43 H. Lu and R. Long, Spin–Orbit Coupling Notably Retards Non-radiative Electron–Hole Recombination in Methylammonium Lead Triiodide Perovskites, *J. Phys. Chem. Lett.*, 2023, **14**, 2715–2721.

44 H. Kim, S. R. Bae, T. H. Lee, H. Lee, H. Kang, S. Park, H. W. Jang and S. Y. Kim, Enhanced Optical Properties and Stability of CsPbBr3 Nanocrystals Through Nickel Doping, *Adv. Funct. Mater.*, 2021, **31**, 1–9.

45 F. Bertolotti, L. Protesescu, M. V. Kovalenko, S. Yakunin, A. Cervellino, S. J. L. Billinge, M. W. Terban, J. S. Pedersen, N. Masciocchi and A. Guagliardi, Coherent Nanotwins and Dynamic Disorder in Cesium Lead Halide Perovskite Nanocrystals, *ACS Nano*, 2017, **11**, 3819–3831.

46 T. Runčevski and C. M. Brown, The Rietveld Refinement Method: Half of a Century Anniversary, *Cryst. Growth Des.*, 2021, **21**, 4821–4822.

47 S. Bera, R. K. Behera and N. Pradhan, α-Halo Ketone for Polyhedral Perovskite Nanocrystals: Evolutions, Shape Conversions, Ligand Chemistry, and Self-Assembly, *J.*

Am. Chem. Soc., 2020, **142**, 20865–20874.

48 K. K. Rohatgi-Mukherjee, Fundamentals of Photochemistry, *Wiley*, 1978.

49 J. R. Lakowicz, Principles of Fluorescence Spectroscopy. 3rd ed.; Springer, 2006.

50 H. Singh and B. Bagchi, Non-Förster distance and orientation dependence of energy transfer and applications of fluorescence resonance energy transfer to polymers and nanoparticles: How accurate is the spectroscopic ruler with 1/R6 rule?, *Curr. Sci.*, 2005, **89**, 1710–1719.

51 S. Saini, G. Srinivas and B. Bagchi, Distance and orientation dependence of excitation energy transfer: From molecular systems to metal nanoparticles, *J. Phys. Chem. B*, 2009, **113**, 1817–1832.

52 K. Zheng, K. Žídek, M. Abdellah, N. Zhu, P. Chábera, N. Lenngren, Q. Chi and T. Pullerits, Directed Energy Transfer in Films of CdSe Quantum Dots: Beyond the Point Dipole Approximation, *J. Am. Chem. Soc.*, 2014, **136**, 6259–6268.

53 M. D. Peterson, S. C. Jensen, D. J. Weinberg and E. A. Weiss, Mechanisms for Adsorption of Methyl Viologen on CdS Quantum Dots, *ACS Nano*, 2014, **8**, 2826–2837.

54 X. Wu, S. Xie, C. Liu, C. Zhou, J. Lin, J. Kang, Q. Zhang, Z. Wang and Y. Wang, Ligand-Controlled Photocatalysis of CdS Quantum Dots for Lignin Valorization under Visible Light, *ACS Catal.*, 2019, **9**, 8443–8451.

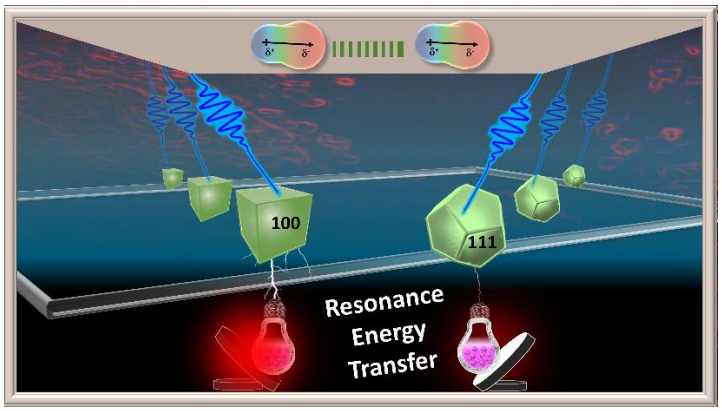

"TOC Graphic"